Scanning nonreciprocity spatial four-wave mixing process in moving photonic band gap

2017 Laser Phys. 27 035402

(http://iopscience.iop.org/1555-6611/27/3/035402)

IOP Publishing | Astro Ltd Laser Physics

Laser Phys. **27** (2017) 035402 (9pp) doi:10.1088/1555-6611/aa5899

Scanning nonreciprocity spatial four-wave mixing process in moving photonic band gap

Hang Wang, Yunzhe Zhang, Mingyue Li, Danmeng Ma, Ji Guo, Dan Zhang and Yanpeng Zhang

Key Laboratory for Physical Electronics and Devices of the Ministry of Education & Shaanxi Key Laboratory of Information Photonic Technique, Xi'an Jiaotong University, Xi'an 710049, People's Republic of China

E-mail: ypzhang@mail.xjtu.edu.cn

Received 6 December 2016, revised 3 January 2017
Accepted for publication 5 January 2017
Published 25 January 2017

Abstract

We experimentally investigate the scanning nonreciprocity of four-wave mixing process induced by optical parametric amplification in moving photonic band gap, which is different from the propagation nonreciprocity in the optical diode. Meanwhile the frequency offset and the intensity difference are observed when we scan the frequency of the beams on two arm ramps of one round trip. Such scanning nonreciprocities can be controlled by changing the frequency detuning of the dressing beams. For the first time, we find that the intensity difference can cause the nonreciprocity in spatial image. In the nonreciprocity process, the focusing or defocusing is resulted from the feedback dressing self-phase modulation while shift and split is attributed to feedback dressing cross-phase modulation. Our study could have a potential application in the controllable optical diode.

Keywords: nonlinear optics, four-wave mixing, fluorescence, bistability, Kerr effect, self-focusing

(Some figures may appear in colour only in the online journal)

1. Introduction

Electromagnetically induced transparency (EIT) [1] can weaken the absorption of the incident light beams in the multilevel atomic system, while electromagnetically induced absorption (EIA) can strengthen the absorption. Under the EIT or EIA condition, the suppression or the enhancement [2–4] can be observed in the four-wave mixing (FWM) [5].

In FWM process, the electromagnetically induced grating (EIG) is resulted from two counter propagating beams [6–8]. The EIG possessing photonic band gap (PBG) structure has a potential application in all optical switch, EIG can be manipulated by the propagation of light to create a tunable photonic band gap [9, 10], due to the strong standing coupling beams, the nonreciprocity phenomenon, resembles optical bistability (OB), has also been demonstrated without a cavity using degenerate FWM in atomic vapor [11, 12]. While there is attention to all-optical diode based on a 'moving' PBG generated in a three level EIT medium in which the propagation nonreciprocity (PN) is observed as the propagation direction of the incident beams is variable [13]. Moreover, PN is also investigated in the optical made of three-level cold ^{87}Rb atoms [14]. In a tradition optical diode based on the PN a signal's transmission is 100% in the forward direction while it vanishes for backward propagation.

In addition the feedback dressing resulted from optical parametrical amplification (OPA) FWM process in an optical cavity have been studied experimentally [15] and theoretically [16], which provides the explanation of the scanning nonreciprocity (SN) in our paper.

Recently, many researchers have shown their interests to the characteristics of the spatial image in the FWM process. Spatially shift and split of one weak laser beam caused by cross-phase modulation (XPM) in Kerr nonlinear optical

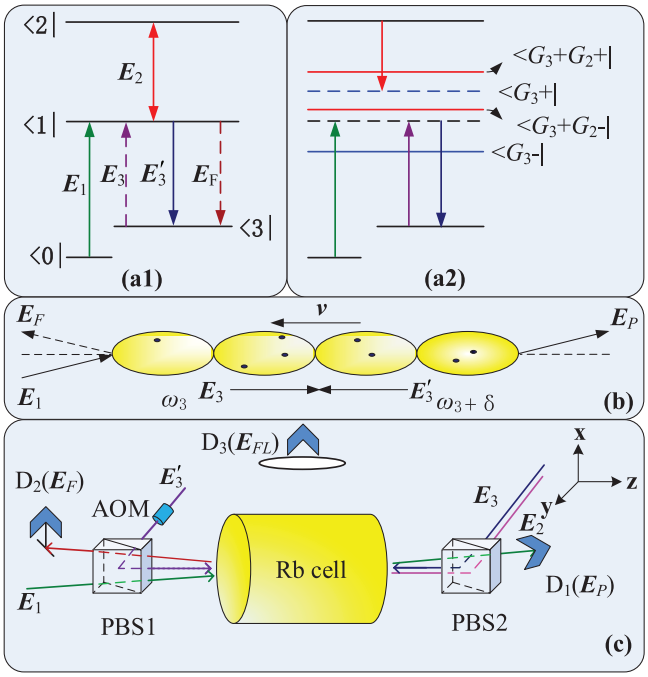

Figure 1. (a1) The cascade four-level atomic system and the involved light beams. (a2) Dressed energy level schematic diagrams. (b) Periodically static standing wave pattern. (c) Setup of our experiment. PBS, polarizing beam splitters; $\boldsymbol{E}_1$, $\boldsymbol{E}_2$, $\boldsymbol{E}_3$ and $\boldsymbol{E}_3'$, laser beams, $\boldsymbol{E}_P$: PTS, $\boldsymbol{E}_F$: FWM signal, $\boldsymbol{E}_{FL}$: fluorescence signal; *D*1–*D*3, detectors; AOM (acousto-optical modulators).

media were studied in early 90s [17, 18]. While there are also studies on the Laser beam self-focusing resulted from self-phase modulation (SPM) [19–21].

In this paper, we investigate the SN of the moving PBG by fixing the propagation direction and the frequency of the incident beam in a reverted-Y type four-level atomic system. The SN caused by OPA refers that the generated signals cannot be overlapped when the signals on the rising ramp (scanning the signal from low frequency to high) and the falling ramp (scanning the signal from high frequency to low) are folded, which is a nonreciprocity under two different scanning mode. Based on the SN and PN in the PBG we can obtain a controllable optical diode in which successful transmission of the signal requires two conditions: the forward direction of the incident signal and the specific scanning mode and frequency of the external dressing signal. Thus the optical diode is controllable and more likely an optical thyristor. Meanwhile, the SN in the spatial image is studied, in other words, the difference in focusing, shift and split between two arm ramps. These phenomenon are explained by combining the theories of intensity difference and SPM (XPM).

2. Experimental setup

The experiment is performed in a reverted-Y type four-level atomic system composed of $5S_{1/2}(F=3)$ ($|0\rangle$), $5S_{1/2}(F=2)$ ($|1\rangle$), $5P_{3/2}$ ($|2\rangle$), and $5D_{5/2}$ ($|3\rangle$) of ^{85}Rb as shown in figure 1(a). Coupling laser beams $\boldsymbol{E}_3$ and $\boldsymbol{E}_3'$ connect the transition $|3\rangle \rightarrow |1\rangle$, the laser beam $\boldsymbol{E}_2$ connects $|1\rangle \rightarrow |2\rangle$, and the probe laser beam $\boldsymbol{E}_1$ connects $|0\rangle \rightarrow |1\rangle$. For a light beam $\boldsymbol{E}_i$ ($i = 1, 2, 3, 3'$), ω_i is the respective laser frequency, $\boldsymbol{k}_i$ is the wave vector, $G_i = \mu_i \boldsymbol{E}_i/\hbar$ is the Rabi frequency with a transition dipole moment μ_i, P_i is the power of laser and Δ_i is the frequency detuning, where $\Delta_i = \Omega_i - \omega_i$. Ω_i is the resonant frequency, Ω_1, Ω_2 and Ω_3 are used for transitions $|0\rangle \rightarrow |1\rangle$, $|1\rangle \rightarrow |2\rangle$ and $|3\rangle \rightarrow |1\rangle$ respectively.

The experiment is performed in a reverted-Y type four-level atomic system composed of $5S_{1/2}(F=3)$ ($|0\rangle$), $5S_{1/2}(F=2)$ ($|1\rangle$), $5P_{3/2}$ ($|2\rangle$), and $5D_{5/2}$ ($|3\rangle$) of ^{85}Rb as shown in figure 1(a). Coupling laser beams $\boldsymbol{E}_3$ and $\boldsymbol{E}_3'$ connect the transition $|2\rangle \rightarrow |1\rangle$, the laser beam $\boldsymbol{E}_2$ connects $|1\rangle \rightarrow |2\rangle$, and the probe laser beam $\boldsymbol{E}_1$ connects $|0\rangle \rightarrow |1\rangle$. For a light beam $\boldsymbol{E}_i$ ($i = 1, 2, 3, 3'$), ω_i is the respective laser frequency, $\mathbf{k}_i$ is the wave vector, $G_i = \mu_i \boldsymbol{E}_i/\hbar$ is the Rabi frequency with a transition dipole moment μ_i, P_i is the power of laser and Δ_i is the frequency detuning, where $\Delta_i = \Omega_i - \omega_i$. Ω_i is the resonant frequency, Ω_1, Ω_2 and Ω_3 are used for transitions $|0\rangle \rightarrow |1\rangle$, $|1\rangle \rightarrow |2\rangle$ and $|3\rangle \rightarrow |1\rangle$ respectively.

Figure 1(c) shows experimental setup. Using the acousto-optical modulators (AOM), we can change ω_3' to get a moving photonic band gap. The PTS ($\boldsymbol{E}_P$) and the generated FWM signal ($\boldsymbol{E}_F$) (which is generated when it satisfies the phase-matching condition $\boldsymbol{k}_F = \boldsymbol{k}_3 + \boldsymbol{k}_1 - \boldsymbol{k}_3'$)and FLS ($\boldsymbol{E}_{FL}$) can be detected by D_1–D_3, respectively. The coupling periodic dressing beams $\boldsymbol{E}_3$ and $\boldsymbol{E}_3'$ propagating through the ^{85}Rb vapor in opposite directions form a moving band gap, it can be dressed by the dressing beam $\boldsymbol{E}_2$, the probe beam $\boldsymbol{E}_1$ propagates along the same direction as $\boldsymbol{E}_3'$ with a small angle between them and the dressing beam $\boldsymbol{E}_2$ propagates in the opposite direction to $\boldsymbol{E}_3'$ with a small angle between them.

3. Basic theory

3.1. Probe transmission signal (PTS), FWM and FLS with feedback dressing

Here we describe feedback models of the $\boldsymbol{E}_P$ and $\boldsymbol{E}_F$. The perturbation chain of FWM BGS can be written as $\rho_{00}^{(0)} \rightarrow \rho_{10}^{(1)} \rightarrow \rho_{20}^{(2)} \rightarrow \rho_{10}^{(3)}$. According to the energy system and Liouville pathways, when the coupling beams frequency $\omega_3 \neq \omega_3'$, the moving first-order and third-order density matrix elements are as follow:

$$\rho_{10}^{(1)} = \frac{\mathrm{i}G_1}{d_1} \tag{1}$$

$$\rho_{10}^{(3)} = \frac{-\mathrm{i}G_1 G_3 G_3'}{d_1 d_2' d_3} \tag{2}$$

Where $d_1 = \Gamma_{10} + \mathrm{i}\Delta_1$, $d_2 = \Gamma_{20} + \mathrm{i}(\Delta_1 + \Delta_2)$, $d_3 = \Gamma_{30} + \mathrm{i}(\Delta_1 - \Delta_3)$, $d_1' = \Gamma_{10} + \mathrm{i}(\Delta_1 - \delta)$, Γ_{ij} is the transverse relaxation rate between states $|i\rangle$ and $|j\rangle$, considering the feedback dressing effect of $\boldsymbol{E}_i$ ($i = 1, 2, 3, 3'$), the first-order and third-order density elements can be write as:

$$\rho_{10}^{(1)} = \frac{iG_1}{d_1 + |G_3|^2/d_3 + |G_2|^2/d_2 + |G_{1T}|^2/\Gamma_{00}} \quad (3)$$

$$\rho_{10}^{(3)} = \frac{-iG_1G_3G_3'}{(d_1 + |G_3|^2/d_3 + |G_2|^2/d_2 + |G_{FR}|^2/\Gamma_{00})^2 d_3} \quad (4)$$

Where $|G_{1T}|^2/\Gamma_{00}$ and $|G_{FR}|^2/\Gamma_{00}$ are the feedback dressing terms resulted from OPA, which can cause the SN. G_{1T} and G_{FR} are the feedback dressing Rabi frequency of PTS and FWM respectively (identified in equations (1) an (2) in [22]). The effect of these feedback dressing terms on PTS or FWM is similar to that of G_2 and G_3.

For the fluorescence signals (FLS), the second-order fluorescence FL_{R1} is described by $\rho_{00}^{(0)} \overset{E_1}{\rightarrow} \rho_{10}^{(1)} \overset{E_1^*}{\rightarrow} \rho_{11}^{(2)}$, so $\rho_{11}^{(2)}$ can be written as:

$$\rho_{11}^{(2)} = -|G_1|^2/d_1\Gamma_{11} \quad (5)$$

when beam $\boldsymbol{E}_2$ is on, the fluorescence process FL_{R1} is dressed and the expression of $\rho_{11}^{(2)}$ can be modified as:

$$\rho_{11}^{(2)} = \frac{-|G_1|^2}{\Gamma_{11}(d_1 + |G_3|^2/d_3 + |G_2|^2/d_2 + |G_{FL}|^2/\Gamma_{00})} \quad (6)$$

$|G_{FL}|^2/\Gamma_{00}$ is the feedback dressing term caused by radiation trap (identified in equation (3) in [22]). Via Liouville pathway $\rho_{00}^{(0)} \overset{E_1}{\rightarrow} \rho_{10}^{(1)} \overset{E_2}{\rightarrow} \rho_{20}^{(2)} \overset{E_1^*}{\rightarrow} \rho_{21}^{(3)} \overset{E_2^*}{\rightarrow} \rho_{22}^{(4)}$, we can obtain the density-matrix element of fourth-order fluorescence (FL_{R2}) signal as:

$$\rho_{22}^{(4)} = \frac{|G_1|^2|G_2|^2}{\Gamma_{22}d_1d_{21}d_5} \quad (7)$$

where $d_5 = \Gamma_{21} + i\Delta_2$. Considering the dressing effect, the dressed density-matrix element of FL_{R2} is given as:

$$\rho_{22}^{(4)} = \frac{|G_1|^2|G_2|^2}{\Gamma_{22}(d_1 + |G_{FL2}|^2/\Gamma_{00})(d_2 + |G_2|^2/d_2)d_5} \quad (8)$$

where $|G_{FL2}|^2/\Gamma_{00}$ is the feedback dressing term caused by radiation trap. The intensity of the signals can be derived from the density-matrix element.

3.2. Theoretical model of the spatial nonlinear propagation of probe and FWM beams

The propagation equations giving the mathematical description of the self- and cross-phase modulation (SPM and XPM) induced spatial interplay of the probe and FWM beams are

$$\frac{\partial u_P}{\partial Z} - \frac{i\partial^2 u_P}{2\partial\zeta^2} = \frac{ik_P^2\omega_0^2 I}{n_0}(n_2^{S1}|u_P|^2 + 2n_2^{X1}|u_1|^2 + 2n_2^{X2}|u_2|^2 + 2n_2^{X3}|u_3|^2 + 2n_2^{X4}|u_3'|^2)u_P \quad (9)$$

$$\frac{\partial u_F}{\partial Z} - \frac{i\partial^2 u_F}{2\partial\zeta^2} = \frac{ik_F^2\omega_0^2 I}{n_0}(n_2^{S2}|u_F|^2 + 2n_2^{X5}|u_1|^2 + 2n_2^{X6}|u_2|^2 + 2n_2^{X7}|u_3|^2 + 2n_2^{X8}|u_3'|^2)u_F \quad (10)$$

where $Z = z/L_D$ ($L_D = k_1\omega_0^2$ is the diffraction length and ω_0 is the spot size of probe beam), with z being the longitudinal coordinate in the propagation direction; $\zeta = x/\omega_0$ and y/ω_0 are the horizontal and vertical coordinates in transverse dimension, respectively; $k_P = k_F = \omega_1 n_0/c$ is the wave vector of PTS and FWM, with n_0 being the refractive index; $n_2^{S1,S2}$ are the self-Kerr coefficients of $\boldsymbol{E}_{P,F}$; n_2^{X1-X8} are the cross-Kerr coefficients of $\boldsymbol{E}_{P,F}$ induced by $\boldsymbol{E}_1$, $\boldsymbol{E}_2$ and $\boldsymbol{E}_3(\boldsymbol{E}_3')$; $u_P = E_P/I^{1/2}$, $u_1 = E_1/I^{1/2}$, $u_2 = E_2/I^{1/2}$, $u_3 = E_3/I^{1/2}$ and $u_3' = E_3'/I^{1/2}$ are the normalized amplitudes of the beams $\boldsymbol{E}_{P,F}$, for simplicity, the intensities of the beams $\boldsymbol{E}_1$, $\boldsymbol{E}_2$ and $\boldsymbol{E}_3(\boldsymbol{E}_3')$ are assumed to be I (they can be further distinguished out by the intensities of I_1, I_2 and $I_3(I_3')$, respectively). On the left sides of equations (9) and (10), the first terms of the both equations describe the beams longitudinal propagation, and the second terms give the diffraction of the beams during propagation. On the right hand sides, the first terms describe the nonlinear self-Kerr effects, and the second to the fifth terms describe the nonlinear cross-Kerr effects.

All the Kerr nonlinear coefficient can be described by a general form $n_2 \approx \mathrm{Re}\tilde{p}_{10}^{(3)}/\varepsilon_0 c n_0$ ($\Delta n_2 = n_2|I_i|^2$). The element $\tilde{p}_{10}^{(3)}$ can be obtained by solving the coupled density-matrix equations, e.g.:

$$\tilde{p}_{10a}^{(3)} = \frac{-iG_{P,F}|G_{P,F}|^2}{\Gamma_{00}(d_1 + |G_1|^2/\Gamma_{00} + |G_2|/d_2 + |G_3|/d_3)^2} \quad (11)$$

for $n_2^{S1,2}$ (induced by $\boldsymbol{E}_{P,F}$)

$$\tilde{p}_{10b}^{(3)} = \frac{-iG_{P,F}|G_1|^2}{\Gamma_{00}(d_1 + |G_1|^2/\Gamma_{00} + |G_2|/d_2 + |G_3|/d_3)^2} \quad (12)$$

for $n_2^{X1,5}$ (induced by $\boldsymbol{E}_1$)

$$\tilde{p}_{10c}^{(3)} = \frac{-iG_{P,F}|G_2|^2}{\Gamma_{00}(d_1 + |G_1|^2/\Gamma_{00} + |G_2|/d_2 + |G_3|/d_3)^2} \quad (13)$$

for $n_2^{X2,6}$ (induced by $\boldsymbol{E}_2$)

$$\tilde{p}_{10d}^{(3)} = \frac{-iG_{P,F}|G_3|^2}{\Gamma_{00}(d_1 + |G_1|^2/\Gamma_{00} + |G_2|/d_2 + |G_3|/d_3)^2} \quad (14)$$

for $n_2^{X3,7}$ (induced by $\boldsymbol{E}_3$).

Equations (11)–(14) proportionally determine the self-Kerr effect induced by $\boldsymbol{E}_{P,F}$ themselves and the cross-Kerr effects induced by $\boldsymbol{E}_1$, $\boldsymbol{E}_2$ and $\boldsymbol{E}_3$ respectively. Thus, n_2 is the superposition of $n_2^{S1,2} = n_2^{SE}$, $n_2^{X1,5} = n_2^{XE_1}$, $n_2^{X2,6} = n_2^{XE_2}$ and $n_2^{X3,7} = n_2^{XE_3}$. If the diffraction and SPM terms are neglected, the solutions of equations (9) and (10) are obtained as:

$u_{\mathrm{P,F}}(z,\xi) = u_{\mathrm{P,F}}(0,\xi)\sum \exp(\mathrm{i}\phi_i)$ $(i = 1, 2, 3)$, where $\phi_i = 2k_{\mathrm{P,F}} z n_2^{XE_i} I_i \mathrm{e}^{-(\xi-\xi_i)^2/2}/(n_0 I_{\mathrm{P,F}})$ is nonlinear phase shift introduced by the strong beam $\boldsymbol{E}_i$, with ζ_i being the central coordinate of $\boldsymbol{E}_i$ in the transverse dimension relative the central coordinate of $\boldsymbol{E}_{\mathrm{P,F}}$ as original point. Therefore, the additional transverse propagation wave-vector introduced by $\boldsymbol{E}_i$ is $\delta k'_{i\xi} = (\partial\phi_i/\partial\xi)\widehat{\xi}$, where $\widehat{\xi}$ is the unit vector along the transverse axis. The direction of $\delta k'_{i\xi}$ determines the $\boldsymbol{E}_i$-induced spatial characteristics change of $\boldsymbol{E}_{\mathrm{P,F}}$ in the transverse dimension, for example $\delta k'_{\mathrm{P},3x} > 0$ shows the $\boldsymbol{E}_3$-induced x direction attraction of $\boldsymbol{E}_{\mathrm{P}}$. When $n_2^{X_i} > 0$, $\delta k'_{i\xi}$ always points to the beam center of the strong beams, the weak beams shift to the strong beams. When $n_2^{X_i} < 0$, the weak beams shift away from the strong beam, when $n_2^{S_i} > 0$ the weak beam is focusing, otherwise the weak beam is defocusing. Moreover, nonlinear phase shift shows the stronger spatial focusing or defocusing, while the shift and splitting can be introduced with larger nonlinear refractive index $\Delta n_2^{E_i} = n_2^{E_i} I_i$ $(i = 1, 2, 3)$ and lower $I_{\mathrm{P,F}}$.

3.3. The frequency offset, intensity difference and spatial characteristics difference between two SN signals

Because of the OPA or radiation trap, the feedback dressing terms in equations (3), (4), (6) and (8) are different on two arm ramps. So the intensities of the observed signals (PTS, FWM BGS and FLS) are different on the rising ramp and the falling ramp.

The frequency offset ($\Delta\nu$) is the horizontal distance between the peaks (dips) on two arm ramps, which can be written as:

$$N(n_{2\mathrm{up}} I_{\mathrm{up}} - n_{2\mathrm{down}} I_{\mathrm{down}}) = \Delta\nu n_0/\omega \tag{15}$$

where I_{up} and I_{down} are the feedback dressing intensities of the signals on the two arm ramps of one single round; ω is the frequency of the observed signal; n_0 is the linear refraction index; N is the atomic density, respectively. If we consider the nonlinear refraction index on the two arm ramps as $n_{2\mathrm{up}} \approx n_{2\mathrm{down}} \approx n_2$, then the equation (15) can be changed into:

$$N n_2 (I_{\mathrm{up}} - I_{\mathrm{down}}) = \Delta\nu n_0/\omega \tag{16}$$

As the feedback dressing effect is different on two arm ramps, the intensities ($I_{\mathrm{P,F}}$) of the PTS or FWM signal are also different. Since the nonlinear refractive coefficient n_2 is the superposition of the SPM refractive coefficient $n_2^{SE_{\mathrm{P,F}}}$ and the XPM refractive coefficient $n_2^{XE_i}$ $(i = 1, 2, 3)$. According to equations (11) and (12)–(14) the intensity difference can cause the change of $n_2^{SE_{\mathrm{P,F}}}$ and $n_2^{XE_i}$ on two arm ramps. So when we study the spatial characteristics of the image, we just consider $n_2^{SE_{\mathrm{P,F}}}$ or $n_2^{XE_i}$ which plays a vital role in the SN process. As the focusing nonreciprocity can be explained by the SPM under the feedback dressing condition. For split and shift in the two arm ramps, $\phi_{i,\mathrm{up}} = 2k_{\mathrm{P,F}} z n_{2\mathrm{up}}^{XE_i} I_i \mathrm{e}^{-(\xi-\xi'_i)^2/2}/(n_0 I_{\mathrm{up}})$ and $\phi_{i,\mathrm{down}} = 2k_{\mathrm{P,F}} z n_{2\mathrm{down}}^{XE_i} I_i \mathrm{e}^{-(\xi-\xi'_i)^2/2}/(n_0 I_{\mathrm{down}})$ are different. So the effect of the strong beam to the PTS or FWM will be different between the rising and the falling ramp.

4. Experimental results and discussions

In this part, the SN phenomenon is investigated by changing the frequency detunings of strong beams. When we scan the frequency detuning Δ_2 in the rising ramp and falling ramp then fold the signals along with the turning point. By comparing the difference of the signals on two ramps, we can describe SN phenomenon, which is different from the PN observed in optical diode made from moving photonic crystal [12]. In an optical diode, due to the Doppler Effect, the frequency of the incident beam is mutative, causing the PN (figure 2 from [12]). But in our experiment, the frequency of the incident light beam is fixed and frequency of the external dressing light beam is scanned, so that one can control the transmission of the incident beam by scanning the frequency of the external dressing beam. In figure 2, the SN behaviour is studied by comparing the signals (PTS FWM and FLS) on the rising (left curves) and falling ramp (right curves). It is easy to find that the signals of the two arm ramps are non-overlapping in x direction and we call it frequency offset ($\Delta\nu$). Meanwhile, there is intensity difference between two arm ramps.

Here, we analyze SN behavior of the PTS in figure 2(a) versus Δ_2 with $\Delta_1 = 70$ MHz at different discrete Δ_3. The background is the dressed PBG signal due to the dressing effect of the strong beam $\boldsymbol{E}_3$. The peaks on the baseline are the EIT satisfying $\Delta_1 + \Delta_2 = 0$ (two photon resonance) according to the term $\left|G_2\right|^2/d_2$ in equation (3). We can see that the peaks on the falling ramp are higher than that on the rising ramp, which we call intensity difference. The difference between the feedback dressing terms $\left|G_{1T}\right|^2/\Gamma_{00}$ of two arm ramps causes the intensity difference. Moreover according to equation (16) the difference between I_{up} and I_{down} can cause $\Delta\nu \neq 0$ so there is frequency offset. We can also find that the frequency offset $\Delta\nu$ changed from 30 MHz (figure 2(a1)) to 25 MHz (figure 2(a2)) and then 20 MHz (figure 2(a3)) as Δ_3 gets larger. Since the nonlinear refractive index n_2 is related to Δ_3, n_2 will get smaller with the change of Δ_3, so the value of $Nn_2(I_{\mathrm{up}} - I_{\mathrm{down}})$ become smaller, according to equation (16) the frequency offset ($\Delta\nu$) will be smaller. So the term $(I_{\mathrm{up}} - I_{\mathrm{down}})$ can cause the frequency offset, and the value of $\Delta\nu$ is mainly determined by n_2. As Δ_1 is fixed at -70 MHz, the feedback dressing effect resulting in the intensity difference and the frequency offset in our experiment is from OPA, SN is different from PN.

For FWM BGS in figures 2(b1)–(b3), the dip on the baseline is resulted from the EIT of PTS as the FWM BGS is the reflected signal of the PBG structure. It is deepest in figure 2(b2) where it satisfies the condition $\Delta_1 - \Delta_3 = 0$ according to $\left|G_3\right|^2/\mathrm{d}_3$ in equation (4). The SN of the FWM BGS can be observed in figure 2(b), it is easy to find the intensity of the signal on the rising ramp is weaker than that on the falling ramp, there is frequency offset, which decreases as Δ_3 becomes larger. Similar to the case in figure 2(a), the intensity difference can be explained by the different feedback dressing

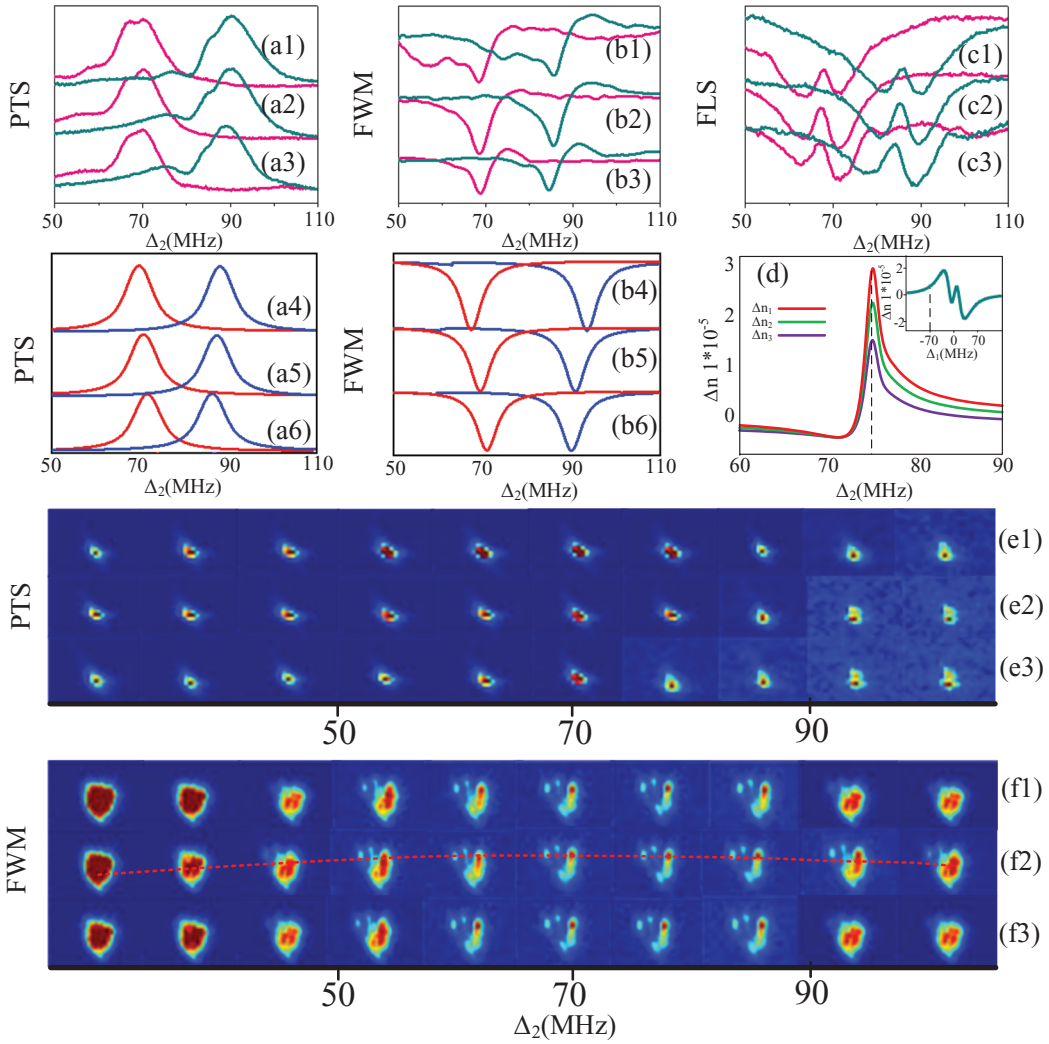

Figure 2. (a) shows the intensities of PTS versus Δ_2 at $\Delta_1 = -70$ with discrete $\Delta_3 = -68$ (a1), -70 (a2) and -72 (a3). (b) and (c) Same as (a) but for FWM and FLS, respectively. Left curves stand for the rising ramp and right curves stand for the falling ramp. (a4)–(a6) and (b4)–(b6) are simulated results of (a1)–(a3), (b1)–(b3), respectively. (d) Inset: the nonlinear refractive index Δn with scanning Δ_1, Δn_1 Δn_2 and Δn_3 are the nonlinear refractive index corresponding to same conditions of (a1)–(a3), respectively; (d) outset: Δn with scanning Δ_2. (e) and (f) The images of $\boldsymbol{E}_{\rm P}$ and $\boldsymbol{E}_{\rm F}$ corresponding to same conditions of (a) and (b), respectively. The dotted line in (f) links the center of the spot and shows the shift of the spatial image.

effect on two arm ramps. The frequency offset occurs because $I_{\rm up} - I_{\rm down} \neq 0$.

For the FLS in figure 2(c), The intensity of the FLS is determined by $\rm FL_{\mathit{R}1}$ and $\rm FL_{\mathit{R}2}$. The dips represent the second-order $\rm FL_{\mathit{R}1}$ appears at the point $\Delta_1 + \Delta_2 = 0$ according to the term $\left|G_2\right|^2/d_2$ in equation (6). Small peak appears at the same point as the fourth-order $\rm FL_{\mathit{R}2}$ dressed by $\boldsymbol{E}_2$ according to the term $\left|G_2\right|^2/d_2$ equation (8). From figure 2(c1) to (c3) the dip becomes deepest in figure 2(c2) when it satisfies $\Delta_2 = -\Delta_1 = -\Delta_3$ (three-photon resonance). There still exists the intensity difference and frequency offset, which can be explained similar to figures 2(a) and (b).

In order to further investigate the spatial character of the PTS and FWM BGS we get their images under the same condition as in figures 2(a) and (b). In this part we only show signals on the rising ramp.

For the PTS (figure 2(e)), one can see the images focus more significantly at $\Delta_2 = 70$ MHz, which is mainly determined by Δn in figure 2(d), because focusing occurs in the $\Delta n > 0$ region and defocusing occurs in the $\Delta n < 0$ region. Near the region $\Delta_2 = 70$ MHz, Δn gets its maximum, so in this region we can observe that the images focus more significantly. For FWM image (figure 2(f)), it also switch from defocusing to focusing and then defocusing. Similarly it can also be explained by the value of Δn. We can notice that near $\Delta_2 = 70$ MHz the FWM beam splitting occurs in the x direction in figure 2(f). This phenomenon can be explained by the relative positions between the weak beams and the strong dressing beams. For the FWM beam $\boldsymbol{E}_{\rm F}$ near the point $\Delta_2 = 70$ MHz the beam shift in the $+y$ direction results from the attraction ($\delta k'_{{\rm F},2y} > 0$) of the strong $\boldsymbol{E}_2$ beam. That makes it get closer to the $\boldsymbol{E}_3$ beam, which can split ($\delta k'_{{\rm F},3x} > 0$) the FWM beam in x direction.

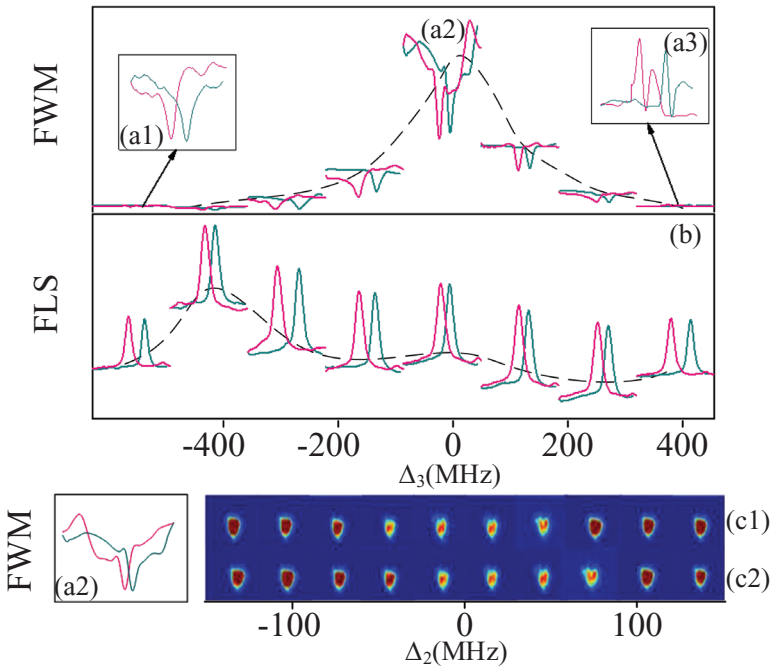

Figure 3. (a) Each sub-curve shows the intensity of FWM versus Δ_2 at $\Delta_1 = 0$ while different sub-curve show the intensity at different discrete Δ_3 from -400 MHz to 400 MHz. (a1) and (a3) The amplified intensity plots of FWM near $\Delta_3 = -400$ MHz and 400 MHz, respectively. (b) The same intensities as (a) but for FLS. (c1) and (c2) The spatial image of rising and falling ramp, respectively, which correspond to same conditions of (a2).

In figure 3, we investigate SN phenomenon by increasing the range of Δ_3 and study the spatial characteristics on the two ramps. When Δ_3 is approaching the larger detuning (figure 3(a3)), we can observe FWM signal changes from suppression to enhancement, simultaneously, SN is observed in the spatial image.

The profile peak of FWM can be described by the dressed enhancement of $\boldsymbol{E}_3$ when it satisfies the resonance condition $\Delta_1 - \Delta_3 = 0$ due to $\left|G_3\right|^2/\mathrm{d}_3$ term in $\rho_{10}^{(3)}$ of equation (4). The dip in each sub-curve is double dressed signal, when Δ_2 is scanned at fixed Δ_3, the FWM signal is suppressed by $\boldsymbol{E}_2$ at the point $\Delta_2 = -\Delta_1$ due to $\left|G_2\right|^2/\mathrm{d}_2$ in equation (4). Here the dip gets deepest at $\Delta_2 = -\Delta_1 = -\Delta_3$ in figure 3(a2) where it satisfies the resonance condition. The dips become shallow as Δ_3 is away from the resonance point, and finally transfer to enhancement peaks when Δ_3 is at large detuning in figure 3(a3). For the FLS in figure 3(b), the profile peak is FL_{R2} signal related to $\rho_{22}^{(4)}$, which is dressed by $\boldsymbol{E}_3$ because of the dressing term $\left|G_{31}\right|^2/\mathrm{d}_3$ in equation (8), in each sub-curve, when Δ_2 is changed, one can find that there exists a peak because the FL_{R2} signal is enhanced by $\boldsymbol{E}_2$. The enhancement becomes strongest at the point $\Delta_1 + \Delta_2 = 0$ according to the $\left|G_2\right|^2/d_2$ in equation (8). Another profile peak appearing in the background at an unexpected position is another second order fluorescence signal from $\boldsymbol{E}_3$ and it is also enhanced by $\boldsymbol{E}_3$ near the point $\Delta_3 = -400$ MHz.

Similar to the figure 2, the dips of the FWM signals on the rising ramp are deeper than those on the falling ramp, which is due to the $\left|G_{\mathrm{FR}}\right|^2/\Gamma_{00}$ in equation (6) is different on the rising ramp and the falling ramp. This difference is due to the feedback dressing effect induced by OPA. The frequency offset $\Delta\nu$ can be explained by $I_{\mathrm{up}} - I_{\mathrm{down}} \neq 0$ according to the equation (16). Then we select one sub-curve in the FWM signal and obtain spatial image (figure 3(c)). And the frequency offset can be observed in the image. We wonder if the SN of other spatial characteristics such as split and shift can be observed in the same way.

In figure 4 the SN is investigated by scanning Δ_2 and setting Δ_1 at different discrete value. In this part we compare the difference of split and shift on two arm ramps. Moreover we also find that the images are switched from y direction split into x direction split.

In detail we get the spatial image figures 4(d) and (e) related to the profiles in figures 4(a) and (b). At $\Delta_1 = -70$ MHz of figures 4(d) and (e), we get the spatial image of PTS and FWM on the rising (figures 4(f1) and (g1)) and falling ramp (figures 4(f2) and (g2)) by scanning Δ_2. This experiment shows the dressing of the strong beams $\boldsymbol{E}_1$ and $\boldsymbol{E}_2$ on the PTS, FWM and FLS. Here we also discuss the difference of split on the rising and falling ramp in figures 4(f) and (g) according to the intensity difference and the XPM. The profile (dash line) in the figure 4(a) shows the background of PTS dressed by $\boldsymbol{E}_1$. The peaks in each sub-curve can be explained by $\boldsymbol{E}_2$ dressing enhancement when it satisfies the condition $\Delta_1 + \Delta_2 = 0$ according to $\left|G_2\right|^2/d_2$ in equation (3). In the region $\Delta_1 < 0$, the peak on the rising ramp is higher while in the region $\Delta_1 > 0$ the peak on the falling ramp is higher, which can be explained by the term $\left|G_{1T}\right|^2/F_{00}$ in the equation (3). When $\Delta_1 < 0$, $\left|G_{1T}\right|^2/F_{00}$ on the rising ramp is smaller than that on the falling

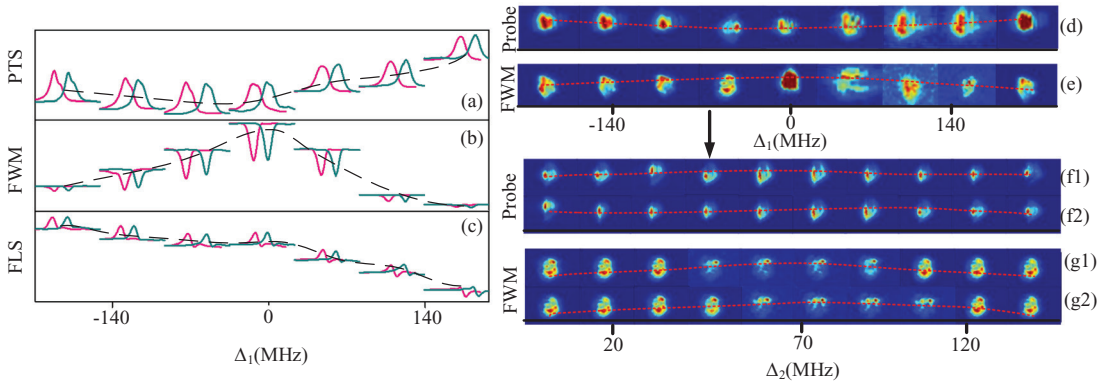

Figure 4. (a) Each sub-curve shows the intensity of PTS versus Δ_2 at $\Delta_3 = 0$ while different sub-curve are at different discrete Δ_1 from -140 MHz to 140 MHz. (b) and (c) The same intensities as (a) but for FWM and FLS, respectively. (d) and (e) The spatial image of PTS and FWM correspond to same conditions of the dash line in (a) and (b), respectively. (f) and (g) are the spatial image of PTS and FWM correspond to same conditions of the sub-curve near the point $\Delta_1 = -70$ MHz in (a) and (b), respectively. (f1) and (g1) Rising ramp; (f2) and (g2) falling ramp. The dotted lines in (d)–(g) link the center of the spot and shows the shift of the spatial image.

ramp which cause the peak in the rising ramp higher; while the similar phenomenon in the region $\Delta_1 > 0$ is also resulted from the term $\left|G_{1T}\right|^2/F_{00}$, which is bigger on the rising ramp.

For the FWM signal in figure 4(b), the profile peak comes from the dressing enhancement of $\boldsymbol{E}_1$ and the dip in each sub-curve represent the suppression of FWM dressed by $\boldsymbol{E}_2$ satisfying $\Delta_1 + \Delta_2 = 0$ according to $\left|G_2\right|^2/d_2$ in equation (4). The deepest dip appears at the point $\Delta_2 = -\Delta_1 = -\Delta_3$ according to the term $\left|G_2\right|^2/d_2 + \left|G_3\right|^2/d_3$ in equation(4). As Δ_1 increases and gets larger detunning, the suppression of the FWM (figure 4(b)) become weaker. For the FLS in figure 4(c) the dash-curve shows background under the dressing effect of $\boldsymbol{E}_1$. When we change Δ_1 from negative to positive, the enhancement condition is transferred to suppression condition, causing the sub-curves changes from peaks to dips.

Now we discuss the spatial characteristics of PTS and FWM. In figures 4(d) and (e) we get the spatial image matching the profile in figures 4(a) and (b). The intensities of the PTS and FWM in the spatial images are corresponding with profiles in figures 4(a) and (b). The images of the PTS and FWM both show the transform from focusing to defocusing, which results from SPM dressed by $\boldsymbol{E}_1$. In the region $\Delta_1 < 0$, $\Delta n^{SE_1} > 0$, so the image is focusing. Near $\Delta_1 = -70$ MHz, Δn^{SE_1} becomes maximum hence the image focuses more significantly. While in the region of $\Delta_1 > 0$, we get $\Delta n^{SE_1} < 0$ and the image is defocusing. Near $\Delta_1 = 70$, Δn^{SE_1} becomes minimum so the image defocuses more significantly. Subsequently, we talk about the shift and split of the images according to the position of the nearby strong beams and the XPM dressed by the nearby the strong beams. The strong beam $\boldsymbol{E}_2$ can cause PTS and FWM shift in $+y$ direction (according to the term $\delta k'_{\mathrm{F},2y}$ or $\delta k'_{\mathrm{P},2y}$). Near $\Delta_1 = 0$ the intensity of PTS gets minimum while the intensity of FWM gets maximum, so the XPM from $\boldsymbol{E}_2$ can be changed according to the equation (13), so the PTS shift to $-y$ direction near $\Delta_1 = 0$ while the FWM shift to the $+y$ direction.

Now we discuss the spatial characteristics of PTS and FWM. In figures 4(d) and (e) we get the spatial image matching the profile in figures 4(a) and (b). The intensities of the PTS and FWM in the spatial images are corresponding with profiles in figures 4(a) and (b). The images of the PTS and FWM both show the transform from focusing to defocusing, which results from SPM dressed by $\boldsymbol{E}_1$. In the region $\Delta_1 < 0$, $\Delta n^{SE_1} > 0$, so the image is focusing. Near $\Delta_1 = -70$ MHz, Δn^{SE_1} becomes maximum hence the image focuses more significantly. While in the region of $\Delta_1 > 0$, we get $\Delta n^{SE_1} < 0$ and the image is defocusing. Near $\Delta_1 = 70$, Δn^{SE_1} becomes minimum so the image defocuses more significantly. Subsequently, we talk about the shift and split of the images according to the position of the nearby strong beams and the

XPM dressed by the nearby the strong beams. The strong beam $\boldsymbol{E}_2$ can cause PTS and FWM shift in $+y$ direction (according to the term $\delta k'_{\mathrm{F},2y}$ or $\delta k'_{\mathrm{P},2y}$). Near $\Delta_1 = 0$ the intensity of PTS gets minimum while the intensity of FWM gets maximum, so the XPM from $\boldsymbol{E}_2$ can be changed according to the equation (13), so the PTS shift to $-y$ direction near $\Delta_1 = 0$ while the FWM shift to the $+y$ direction.

In figures 4(f) and (g), when Δ_2 is scanned at $\Delta_1 = -70$ MHz we investigate SN of spatial image for the PTS and FWM. At first, the frequency offset is observed in the two arm ramps which is similar to our discussion in figure 2(a). For the PTS, the intensity of the spatial image is from weak to strong and then weak, which conforms with the intensity in the sub-curve of figure 4(a). The background of the images focus mainly due to $\Delta n^{SE_1} > 0$ at $\Delta_1 = -70$ MHz. For the FWM (figure 4(g)) it is also in the focusing background and the images focus more significantly with Δn^{SE_1} (SPM dressed by the strong beam $\boldsymbol{E}_2$) getting maximum. Here the PTS image shifts towards $\boldsymbol{E}_2$ along $+y$ direction when $\Delta n^{SE_1} > 0$, $\delta k'_{\mathrm{P},2y} > 0$. At $\Delta_2 = 70$ MHz, Δn^{XE_2} becomes maximum and the shift becomes more significant. Similarly the FWM is also shift in $+y$ direction and follows the same rule as PTS in figure 4(f), which can be explained by the influence of Δn^{XE_2} and $\delta k'_{\mathrm{F},2y}$. One can notice that PTS in figure 4(f) split in x direction and the split occurs in three regions: near $\Delta_2 = 20$, 70 and 140 MHz. PTS shifts in $+y$ direction results from the attraction ($\delta k'_{\mathrm{P},2y} > 0$) of the

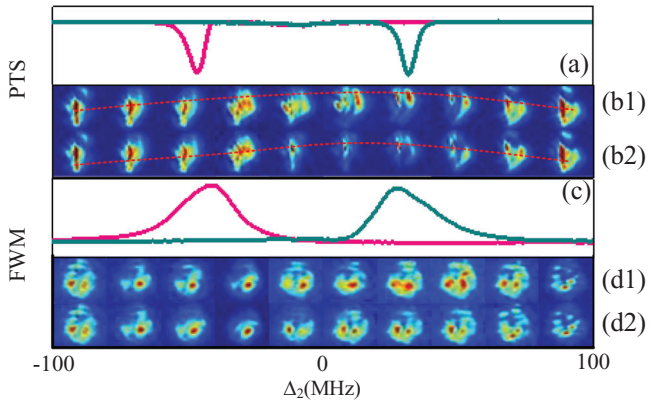

Figure 5. (a) and (c) The intensity of PTS and FWM versus Δ_2 at $\Delta_3 = \Delta_1 = 0$, (b) and (d) the spatial image of PTS and FWM correspond to same conditions of (a) and (c), respectively. (b1) and (d1) Rising ramp; (b2) and (d2) falling ramp. The dotted lines in (b) link the center of the spot and shows the shift of the spatial image.

$\boldsymbol{E}_2$ beam, it gets near to the strong beam $\boldsymbol{E}_1$ and $\boldsymbol{E}_3$, respectively. At $\Delta_2 = 20$ and 140 MHz the split is caused by the strong beam $\boldsymbol{E}_1$ as in this region $\delta k'_{\mathrm{P},1x} > 0$. While at the point $\Delta_2 = 70$ MHz the PTS splits due to the influence of $\boldsymbol{E}_3$ when $\delta k'_{\mathrm{P},3x} > 0$. As PTS and the strong beam $\boldsymbol{E}_2$ does not coincide, the strong beam $\boldsymbol{E}_2$ can only cause the shift but not split of PTS. While in figure 4(g), one can witness that the FWM image initially splits in y direction and then split in x direction. The y direction splitting can be explained by the XPM of $\boldsymbol{E}_2$, when $\delta k'_{\mathrm{F},2y} > 0$, the FWM is attracted by $\boldsymbol{E}_2$, so it can both shift and split. In the region far from $\Delta_2 = 70$, the intensity of FWM is stronger, so the internal stability of FWM (figure 4(g)) is low and it appears to split in y direction. While near $\Delta_2 = 70$ the intensity of FWM becomes weaker and all the spot can be attracted towards $\boldsymbol{E}_2$ as it appears to shift. In figure 4(g), at $\Delta_2 = 70$ the shift is more significant, the FWM get near to the strong beam $\boldsymbol{E}_3$ and at that point $\delta k'_{\mathrm{F},3x} > 0$, which causes the x direction splitting. One can notice that the split in x direction of the FWM near $\Delta_2 = 70$ MHz is more significant on the falling ramp (figure 4(g2)) than that on the rising ramp (figure 4(g1)). As the intensity of the falling ramp is stronger the term G_{F} in equation (14) is bigger on the falling ramp, which means that the attraction from the strong beam $\boldsymbol{E}_3$ is stronger ($\delta k'_{\mathrm{F},3x}$ is larger). On the other hand, when the intensity increases, the internal stability of the beam decreases, so it is easy to split. Hence the intensity difference causes the spatial nonreciprocity.

In figure 5, we focus on the differences of the focusing, split and shift between the rising ramp and the falling ramp in the SN process. In this part we ignore the frequency offset and move the spatial images on the rising ramp (figures 5(b1) and (d1)) in x direction to let them overlap with the image on the falling ramp so that one can find that there are obvious differences in images between the raising and the falling ramp.

For the PTS, one can see the spot is focusing at $\Delta_2 = 20$ MHz, where there exists a dip in figure 5(a). Moreover the dip in the falling ramp is deeper than the dip in the rising ramp due to the influence of $\left|G_{1T}\right|^2/\Gamma_{00}$ in equation (3). So we know at the point $\Delta_2 = 20$ MHz, $\left|G_{\mathrm{P}}\right|^2$ is smaller. According to equation (11) the SPM can cause the $n^{SE_{\mathrm{P}}}$ bigger on the falling ramp than rising ramp, as a result, the focusing phenomenon is more significant at falling ramp (figure 5(b2)). As the intensity of the dip gets weaker, it is easily to be influenced by the nearby strong beams. So near the point $\Delta_2 = 20$ MHz in the spatial image, it appears to be shift. As the intensity of PTS on the falling ramp is weaker, it is easily affected by the nearby strong beams than the signal in the rising ramp at approximately equal Δn, so the PTS beam in the rising ramp shifts more significantly. Since the PTS shifts in $+y$ direction, it gets closer to the strong beam $\boldsymbol{E}_3$, which is at the right side of the PTS. So the effect of the beam $\boldsymbol{E}_3$ get stronger, such that it causes splitting of PTS in x direction due to $\delta k'_{\mathrm{P},3x}$.

For the FWM BGS in figure 5(c), there are peaks on the rising ramp and the falling ramp. Because of the influence of $\left|G_{\mathrm{FR}}\right|^2/\Gamma_{00}$ in the equation (6), the peak on the rising ramp is higher. So one can predict at that point ($\Delta_2 = 20$ MHz) the term $\left|G_{\mathrm{F}}\right|^2$ is smaller on the falling ramp. According equation (13) the SPM can cause the $n^{SE_{\mathrm{F}}}$ to be bigger on the falling ramp than on the rising ramp. Consequently focusing phenomenon is greater on the falling ramp (figure 5(d2)). Since the intensity of the signal gets stronger, the internal stability will decrease so it is easier to split than to shift. As the intensity of the FWM becomes stronger, the term G_{F} in equation (14) is also bigger so $\delta k'_{\mathrm{P},3x}$ is bigger, which means that the attraction from $\boldsymbol{E}_3$ get stronger. In the meantime, the internal stability of FWM gets low because of the stronger intensity, so the spots begin to split in x direction near the point $\Delta_2 = 20$ MHz. The intensity of FWM on the rising ramp is stronger than that on the falling ramp, which means the signal on the rising edge is easier to split. So on the rising ramp, we can observe the y direction split attracted by $\boldsymbol{E}_2$, but no split on the falling ramp. So the intensity difference can cause different SPM and XPM, which can cause the SN in spatial characteristics.

5. Conclusion

In summary, the frequency offset and the intensity difference of PTS, FWM and FLS are caused by feedback dressing resulted from OPA or radiation trap. The propagation direction of the incident beam ($\boldsymbol{E}_1$) is fixed when Δ_1 is fixed, hence the SN in this paper turn out to be different from the PN in an optical diode. Moreover, the intensity difference can cause different SPM (XPM) between two ramps. The SN of focusing is caused by the feedback dressing SPM, while the SN of shift and split of images resulted from the feedback dressing XPM.

Acknowledgment

This work was supported by the 973 Program (2012CB921804), KSTIT of Shaanxi Province (2014KCT-10), NSFC (11474228, 61308015, and 61205112).

References

[1] Harris S E 1997 Electromagnetically induced transparency *Phys. Today* **50** 36–42

[2] Hemmer P R, Katz D P, Donoghue J, Shahriar M S, Kumar P and Cronin-Golomb M 1995 Efficient low-intensity optical phase conjugation based on coherent population trapping in sodium *Opt. Lett.* **20** 982

[3] Li C, Zheng H, Zhang Y, Nie Z, Song J and Xiao M 2009 Observation of enhancement and suppression in four-wave mixing processes *Appl. Phys. Lett.* **95** 041103

[4] Zheng H, Zhang X, Li C, Lan H, Che J, Zhang Y and Zhang Y 2013 Suppression and enhancement of coexisting superfluorescence and multi-wave mixing processes in sodium vapour *J. Chem. Phys.* **138** 204315

[5] Krolikowski W, Saffman M, Luther-Davies B and Denz C 1998 Anomalous interaction of spatial solitons in photorefractive media *Phys. Rev. Lett.* **80** 3240–3

[6] Harris S E, beam J E and Imamoglu A 1990 Nonlinear optical processes using electromagnetically induced transparency *Phys. Rev. Lett.* **64** 1107

[7] Schmidt H and Imamoglu A 1996 Giant Kerr nonlinearities obtained by electromagnetically induced transparency *Opt. Lett.* **21** 1936–8

[8] Boyer V, McCormick C F, Arimondo E and Lett P D 2007 Ultraslow propagation of matched pulses by four-wave mixing in an atomic vapor *Phys. Rev. Lett.* **99** 143601

[9] Brown A W and Xiao M 2005 All-optical switching and routing based on an electromagnetically induced absorption grating *Opt. Lett.* **30** 699–701

[10] Artoni M and La Rocca G C 2006 Optically tunable photonic stop bands in homogeneous absorbing media *Phys. Rev. Lett.* **96** 073905

[11] Gauthier D J, Malcuit M S, Gaeta A L and Boyd R W 1990 Polarization bistability of counterpropagating laser beams *Phys. Rev. Lett.* **64** 1721

[12] Ackemann T, Heuer A, Logvin Y A and Lange W 1997 Light-shift-induced level crossing and resonatorless optical bistability in sodium vapor *Phys. Rev.* A **56** 2321

[13] Wang D, Zhou H, Guo M, Zhang J, Evers J and Zhu S 2013 Optical diode made from a moving photonic crystal *Phys. Rev. Lett.* **110** 093901

[14] Horsley S A R, Wu J, Artoni M and La Rocca G C 2013 Optical nonreciprocity of cold atom bragg mirrors in motion *Phys. Rev. Lett.* **110** 223602

[15] Chen H, Zhang Y, Yao X, Wu Z, Zhang X, Zhang Y and Xiao M 2014 Parametrically amplified bright-state polariton of four- and six-wave mixing in an optical ring cavity *Sci. Rep.* **4** 03619

[16] Zheng H, Zhang X, Zhang Z, Tian Y, Chen H, Li C and Zhang Y 2013 Parametric amplification and cascaded-nonlinearity processes in common atomic system *Sci. Rep.* **3** 01885

[17] Agrawal G P 1990 Induced focusing of optical beams in self-defocusing nonlinear media *Phys. Rev. Lett.* **64** 2487

[18] Hickmann J M, Gomes A S L and de Araujo C B 1992 Observation of spatial cross-phase modulation effects in a self-defocusing nonlinear medium *Phys.Rev. Lett.* **68** 3547

[19] Xiao M, Li Y, Jin S and Gea-Banacloche J 1995 Measurement of dispersive properties of electromagnetically induced transparency in rubidium atoms *Phys. Rev.Lett.* **74** 666

[20] Wang H, Goorskey D and Xiao M 2001 Enhanced Kerr nonlinearity via atomic coherence in a three-level atomic system *Phys. Rev. Lett.* **87** 073601

[21] Sang S, Wu Z, Sun J, Lan H, Zhang Y, Zhang X and Zhang Y P 2012 Observation of angle switching of dressed four-wave mixing image *IEEE Photon. J.* **4** 1973–86

[22] Zhang D, Wang Z, Zhang Y, Abdulkhaleq H, Zhang W, Liu Z and Zhang Y P 2015 Parametrical amplification induced nonreciprocity in photonic band gaps *RSC Adv.* **5** 77372–9